

Research Article

Design of FDM-printable tendon-driven continuum robots using a serial S-shaped backbone structure

Kaidi Zhu, Tim C. Lueth, Yilun Sun*

Institute of Micro Technology and Medical Device Technology, Technical University of Munich, Garching 85748, Germany

ARTICLE INFO

Article history:

Received 20 August 2024

Revised 20 September 2024

Accepted 10 October 2024

Available online 18 October 2024

Keywords:

Continuum robot

FDM printing

Tendon-driven mechanism

Mechanics modeling

ABSTRACT

Tendon-driven continuum robots (TDCR) are widely used in various engineering disciplines due to their exceptional flexibility and dexterity. However, their complex structure often leads to significant manufacturing costs and lengthy prototyping cycles. To cope with this problem, we propose a fused-deposition-modeling-printable (FDM-printable) TDCR structure design using a serial S-shaped backbone, which enables planar bending motion with minimized plastic deformation. A kinematic model for the proposed TDCR structure based on the pseudo-rigid-body model (PRBM) approach is developed. Experimental results have revealed that the proposed kinematic model can effectively predict the bending motion under certain tendon forces. In addition, analyses of mechanical hysteresis and factors influencing bending stiffness are conducted. Finally, a three-finger gripper is fabricated to demonstrate a possible application of the proposed TDCR structure.

© 2024 The Author(s). Published by Elsevier B.V. on behalf of Shandong University. This is an open access article under the CC BY-NC-ND license (<http://creativecommons.org/licenses/by-nc-nd/4.0/>).

1. Introduction

Continuum robotics has attracted increasing interest over the past few years due to its flexible, continuous structures that allow smooth and highly adaptable motion [1,2]. Defined by their ability to bend continuously along their length without discrete joints, continuum robots mimic the flexibility and dexterity of biological organisms, such as the tentacles of an octopus [3], an elephant's trunk [4], or an inchworm [5]. This unique design enables them to achieve a high ratio of length to width [6], making them ideal for minimally invasive surgical applications [7–9], search and rescue missions [10,11], and industrial tasks requiring precise manipulation in confined spaces [12].

Over the last few decades, a large number of research studies have been conducted to design continuum robots. For instance, Webster et al. [13] introduced the concentric tube continuum robot, which consists of multiple nested, pre-curved tubes that can slide and rotate relative to each other. The overall shape and direction of the robot can be controlled by adjusting the relative positions and orientations of the tubes. Despite the advantage of combining small size with enough stiffness, there is a potential snapping problem due to its difficult kinematic analysis [14]. To achieve a smaller scale for continuum robots, Kim et al. [15] and Edelmann et al. [16] incorporated magnetically actuated designs, which utilize magnetic fluid and permanent magnets, respectively. These continuum robots can be controlled in a magnetic

field without any actuation wires, thus eliminating problems caused by friction. However, this type of continuum robot has poor loading capacity and issues with biocompatibility [6]. In [17], Ikuta et al. developed a “soft robot”, which involves constructing the entire robot from flexible, rubbery materials. Shape changes are achieved by incorporating pneumatic or hydraulic chambers within the elongated elements. This design allows the combination of actuation methods and materials from both soft and non-soft continuum robots [6,18]. However, as a result of the low rigidity of the materials, buckling and significant nonlinearities in the kinematic model can occur [19]. Tendon actuation is one of the most commonly adopted strategies for designing continuum robots [20,21] due to its ability to exert large forces, ease of control, and high power-to-weight ratio [19,22]. Tendon-driven continuum robots (TDCR) have a flexible backbone that can bend in multiple directions. Manipulation is realized by pulling a series of tendons routed through the flexible backbone and fixed at its distal end with the TDCR. Most backbones are made of Nitinol or polymers [19]. For instance, the continuum robotic structures in [23–25] were fabricated using PA2200 with selective laser sintering (SLS). Authors in [26] used electrical discharge machining (EDM) to cut notches on the Nitinol backbone and successfully maintained manufacturing tolerances. However, these designs usually face challenges such as long prototyping cycles and high manufacturing costs.

To address the above challenges, fused deposition modeling (FDM) has become a widespread technique in the current state of the art due to its ability to accelerate the development process and cost-effectiveness [27]. FDM generally has a lower

* Corresponding author.

E-mail address: yilun.sun@tum.de (Y. Sun).

manufacturing cost than other 3D-printing techniques due to inexpensive filaments and machines. Ford Motor Company utilizes FDM to create functional prototypes for a wide range of components, including engine parts and interior features [28]. In the medical field, researchers and medical professionals use FDM to create custom prosthetic and anatomical models for surgical planning. The ability of FDM to quickly produce accurate and patient-specific models has revolutionized preoperative procedures, resulting in better surgical outcomes and improved patient care [29,30]. However, one of the major challenges using FDM is that the material parameters are difficult to quantify. In other words, even if the same printing parameters are used across different printers, the mechanical properties of the final product can vary significantly. The reasons for this inconsistency could be variations in printer calibration, material quality, and ambient conditions during printing [31]. Therefore, these issues must be considered during the design and modeling process of FDM-printed continuum robots.

In this article, we propose a FDM-printable TDCR structure, in which a serial S-shaped backbone is utilized to achieve minimum plastic deformation of the continuum robots during the bending motions. This work has the following contributions:

- (1) Mechanical design of an FDM-printable TDCR structure based on a serial S-shaped backbone structure.
- (2) Development of a kinematic model that can be applied to the proposed TDCR with arbitrary structural parameters.
- (3) Model validation and exploration of the influence of structural parameters on bending stiffness through experiments.

The rest of the letter is organized as follows: Section 2 first introduces the mechanical design of the FDM-printable TDCR structure. In Section 3, a kinetostatic analysis based on the pseudo-rigid-body model (PRBM) is conducted to predict its bending motion. Experiments are performed in Section 4 to validate the kinematic model and assess the influence of structural parameters on the bending stiffness. Additionally, a demonstration of the application is presented. Section 5 discusses the proposed TDCR structure in terms of its performance and outlines future work. Section 6 concludes the entire letter.

2. Structural design and fabrication

In this study, we chose polylactic acid (PLA) to fabricate the proposed TDCR structure. PLA is a widely used filament for FDM due to its low cost and biodegradability. It tends to warp less than other materials like ABS, resulting in better dimensional accuracy. Since the design of compliant mechanisms requires materials with high strength and a low Young's modulus [32], PLA's high yield strength to Young's modulus ratio makes it an ideal material for our purposes. However, PLA inherently has a low yield strength, making it prone to plastic deformation. Since the TDCR relies on the backbone's compliance to achieve flexible motion, large plastic deformation is not allowed to occur in order to maintain its functionality. Conventional flexure joints such as leaf-spring or cartwheel type are therefore not ideal for this material. To address this problem, we proposed a serial S-shaped structure as graphically illustrated in Fig. 1.

The proposed TDCR structure is specifically designed to bend within the xy -plane, as the issue of stress concentration is minor in this bending direction. It features a backbone consisting of a serial S-shaped structure with constant line width, which can be further subdivided into multiple identical U-shaped substructures. The backbone includes two opposite threading holes that allow the tendon to pass through, enabling bending about both positive and negative z -direction. Bending motion can be steered by pulling the tendon on one side. The bending angle increases

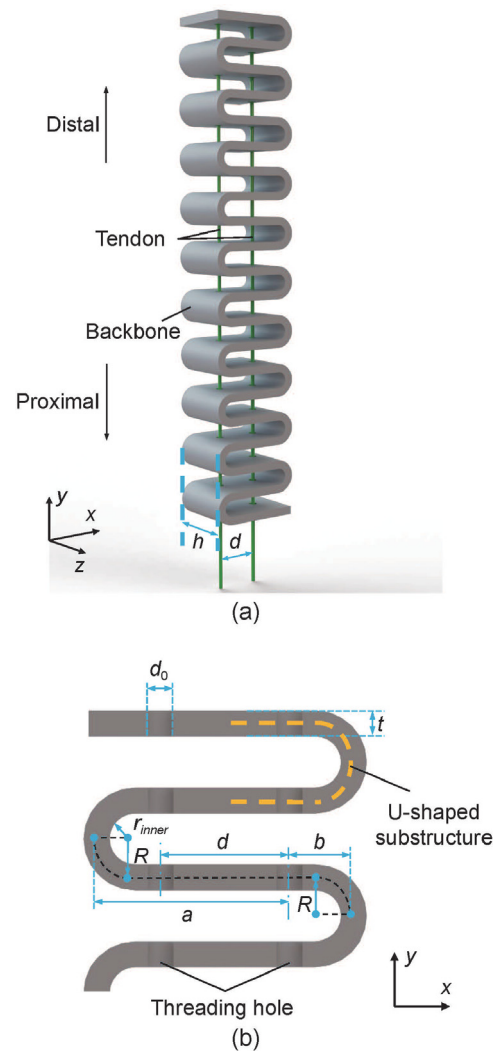


Fig. 1. Schematic illustration of the proposed TDCR structure. (a) Perspective view. (b) Section view.

with the pulling length of the tendon. When the tendon is no longer under tension, the TDCR returns to its initial unbent shape. The distal ends of the tendons are fixed to the tip of the backbone, while the proximal ends can be freely actuated. During actuation, the tensile force in the tendon is transformed into a bending force applied to the backbone. Due to the monolithic design of the TDCR structure, there is no need for assembly within a single segment, eliminating tolerance issues associated with insufficient printing accuracy. With fewer parts, the sterilization process can also be simplified [33]. Additionally, its scalable sizes make it applicable for versatile scenarios.

In this work, the proposed TDCR structure was fabricated by an FDM printer (X1-Carbon 3D printer, Bambu Lab, China) with a nozzle diameter of 0.4 mm using PLA Basic filament (Bambu Lab, China). As mentioned in Section 1, the mechanical property of the print is relevant to the print direction in FDM. Generally, the strength of the printed object in the height direction is lower than that in the horizontal direction. To achieve isotropic mechanical properties within the bending plane, the TDCR structure is placed on the build plate with the xy -plane up and sliced along the z -direction (see Fig. 2), resulting in a consistent pattern for all layers.

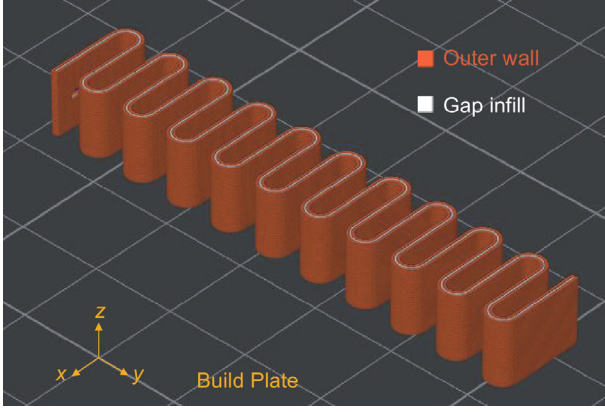


Fig. 2. Sliced 3D-model shows the printing orientation of the TDCR in the FDM printer.

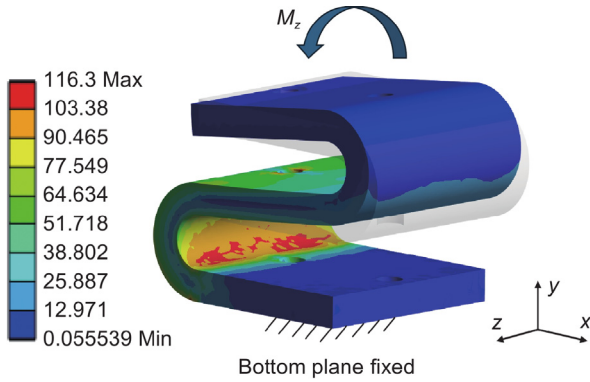


Fig. 3. FEA result shows the von-Mises stress distribution of a single segment of the S-shaped structure under a torque M_z using ANSYS.

3. Mechanics-based kinematic modeling

3.1. Kinetostatic analysis

To develop a kinematic model that can predict the bending shape of the TDCR effectively, we conducted a kinetostatic analysis on the proposed TDCR structure using a pseudo-rigid-body model (PRBM) approach. The PRBM simplifies a flexible continuum mechanism into a system composed of rigid links and pivots, with springs providing the necessary compliance. Considering that the motion of the TDCR is predominantly induced by tendon forces, the effects of gravity and friction are negligible in the modeling process. Due to the TDCR's planar bending motion, the model is reduced to a two-dimensional representation.

Fig. 4 demonstrates the simplified mechanical model of the TDCR structure using the PRBM approach, where the line width is not pictured for brevity. Through FE simulation [34] (as shown in Fig. 3), we found that the largest von-Mises stress occurs in the semicircular-shaped regions of the TDCR during bending, while the stress concentration in the straight-line regions is comparatively low. Therefore, pseudo pivots are intentionally placed in the middle of each semicircular arc in our model. The TDCR structure is segmented into $N+1$ rigid links arranged in series and interconnected via N pseudo pivots. Each rigid link is composed of two (or one for the first ($i = 0$) and the last ($i = N$) rigid link) identical quarter-circle arcs connected by a straight line that is tangent to the arcs. The modeling of stiffness is achieved by integrating torsional springs at each pivot ($i = 1, \dots, N$). Here, the bending stiffness of the entire U-shaped substructure is modeled to be equivalent to the spring constant of the corresponding

torsional spring. Since all U-shaped substructures have identical geometry, all spring constants are modeled to have the same value.

Hence, the torque T_i generated by the torsional spring at the i th pivot (i) can be expressed as

$$T_i = K\theta_i \quad (1)$$

where K is the spring constant, while θ_i corresponds to the bending angle at the i th pivot. Since the first ($i = 0$) and the last rigid link ($i = N$) are not subject to the same bending forces as the others, they need to be analyzed separately. Considering that the first rigid link ($i = 0$) is fixed in our model, it can be omitted from the discussion. For i from 1 to $N-1$, the equilibrium of forces at the i th rigid link can be formulated as

$$\sum \mathbf{F} = {}^0\mathbf{F}_{i,i-1} + {}^0\mathbf{F}_{i,i+1} + {}^0\mathbf{A}_i(\beta_i) {}^i\mathbf{F}_{bi} = \mathbf{0} \quad (2)$$

where ${}^i\mathbf{F}_{bi} = [F_{bi} \ 0]^T$ is the bending force introduced by the tendon acting on the i th rigid link within the local frame \mathbf{e}_i . The coordinate origin of \mathbf{e}_i is set at the i th threading hole P_i , and the x -axis is aligned parallel to the straight-line part of the i th rigid link. As schematically illustrated in Fig. 4, F_{bi} can be determined using the following equation:

$$F_{bi} = 2F_t \cos \varphi_i \quad (3)$$

with

$$\varphi_i = \frac{\pi}{2} - \frac{1}{4}(\theta_{i+1} + \theta_i) \quad (4)$$

${}^0\mathbf{A}_i$ is a rotation matrix used to transform the local frame \mathbf{e}_i to the global frame \mathbf{e}_0 , which takes on the following form:

$${}^0\mathbf{A}_i(x) = {}^i\mathbf{A}_0(x)^T = \begin{bmatrix} \cos x & \sin x \\ -\sin x & \cos x \end{bmatrix} \quad (5)$$

The angle β_i can be calculated as:

$$\beta_i = \alpha_i + \frac{1}{4}(\theta_{i+1} + \theta_i) \quad (6)$$

where

$$\alpha_i = \sum_{k=1}^i \theta_k \quad (7)$$

${}^0\mathbf{F}_{i,i-1} = {}^0[F_{x,i} \ F_{y,i}]^T$ represents the bearing forces exerted by the $i-1$ -th rigid link on the i th rigid link within the global frame \mathbf{e}_0 . For the last rigid link ($i = N$), the equilibrium of forces can be formulated as

$$\sum \mathbf{F} = {}^0\mathbf{F}_{N,N-1} + {}^0\mathbf{A}_N(\psi) {}^N\mathbf{F}_t = \mathbf{0} \quad (8)$$

with

$$\psi = \alpha_N - \frac{\theta_N}{2} + \frac{\pi}{2} \quad (9)$$

where ${}^N\mathbf{F}_t = [F_t \ 0]^T$ is the tendon force expressed in the N th local frame. The x -axis of N th local frame is oriented in the same direction as the tendon's pull.

Next, we derive the equilibrium of moments around the threading hole P_i for the i th rigid link, which can be written as

$$\sum M^{(P_i)} = T_i + T_{i+1} + {}^i\mathbf{r}_{P_i,i} \times {}^i\mathbf{F}_{i,i-1} + {}^i\mathbf{r}_{P_i,i+1} \times {}^i\mathbf{F}_{i,i+1} = 0 \quad (10)$$

with

$${}^i\mathbf{F}_{i,i-1} = {}^i\mathbf{A}_0(\alpha_i) {}^0\mathbf{F}_{i,i-1} \quad (11)$$

where ${}^i\mathbf{r}_{P_i,i}$ represents the lever arm, which is a vector that points from P_i to the coordinate origin of the local frame i within local

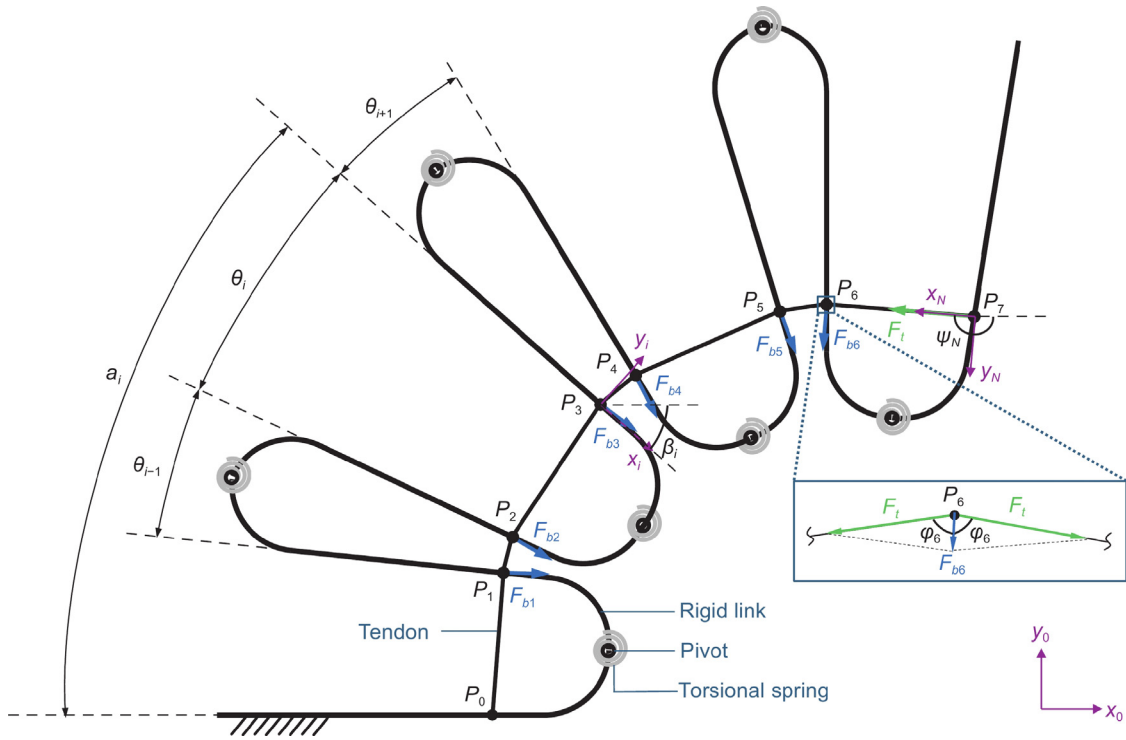


Fig. 4. PRB model of the proposed TDCR structure consisting of 8 rigid links and 7 pivots ($N=7$).

frame \mathbf{e}_i . This formula is applicable to all N rigid links, as T_{N+1} and ${}^i\mathbf{F}_{N,N+1}$ are zero.

Additionally, according to Newton's third law of motion, we have

$${}^0\mathbf{F}_{i,i+1} = -{}^0\mathbf{F}_{i+1,i} \quad (12)$$

and

$$M_{i,i+1} = -M_{i+1,i} \quad (13)$$

By substituting Eqs. (1), (3), (4), (6), (7), (9), (12), and (13) into Eqs. (2), (8) and (10), we obtain a system of nonlinear equations consisting of $3n$ equations and $3n + 5$ unknowns. Thus, a unique solution for θ_i can be calculated as long as the values for the structural parameters R , a , b , the tendon force F_t , as well as the spring constant K are given. Consequently, the vector containing all N bending angles Θ can be expressed as a function as follows:

$$\Theta = f(R, a, b, F_t, K) \quad (14)$$

Once the bending angles θ_i are calculated, the positions of threading holes P_i within the global frame \mathbf{e}_0 can be written as

$${}^0\mathbf{r}_{P_i} = \sum_{k=1}^i s_k \begin{bmatrix} \sin \alpha_k \\ \cos \alpha_k \end{bmatrix} \quad (15)$$

where s_i describes the distance between P_i and P_{i+1} , which can be derived from the geometry of the structure. For the configuration shown in Fig. 4, s_i is given as

$$s_i = \begin{cases} 2R\sqrt{1 + \sin \theta_i} + 2(b - R) \sin \frac{\theta_i}{2}, & i \text{ is odd} \\ 2R\sqrt{1 - \sin \theta_i} - 2(a - R) \sin \frac{\theta_i}{2}, & i \text{ is even} \end{cases} \quad (16)$$

3.2. Calculation of the spring constant

Determining the stiffness of the structure is a crucial part of the design process. However, as previously noted, the mechanical properties of the filament material cannot be directly applied to calculate the mechanical properties of printed objects accurately

Algorithm 1: NLP-Based calculation of the spring constant.

Input: $n, R, a, b, \Theta, F_t, K_0$, tolerance ϵ

Output: K

- 1 Initialize $K \leftarrow K_0$;
- 2 **while** $\mathcal{L} > \epsilon$ **do**
- 3 $\Theta \leftarrow f(R, a, b, F_t, K)$;
- 4 $\mathcal{L} \leftarrow \frac{1}{N} \sum_{i=1}^N (\Theta - \hat{\Theta})^2$;
- 5 $K \leftarrow \text{minimize } \mathcal{L} \text{ s.t. } K > 0$;
- 6 **end**

in FDM. Additionally, since the spring constant K represents the bending stiffness of the entire U-shaped substructure, it is difficult to directly calculate K using the traditional beam theory. Therefore, an alternative approach must be developed to determine the value of K .

In this work, the identification task is converted into a non-linear programming (NLP) problem that includes an inequality constraint as outlined in Algorithm 1. The spring constant K is chosen as the design variable and the design objective is set to minimize the mean squared error (MSE) of the bending angles at all N pivots, which is formulated as follows:

$$\begin{aligned} \min_K & \frac{1}{N} \sum_{i=1}^N (\Theta - \hat{\Theta})^2 \\ \text{s.t.} & K > 0 \end{aligned}$$

In this formulation, Θ is the predicted bending angles calculated according to Eq. (14) and $\hat{\Theta}$ represents the real bending angles measured through experiments. The entire algorithm was implemented in MATLAB and the *fmincon* function was used to solve the minimization problem in step 5 of the Algorithm.

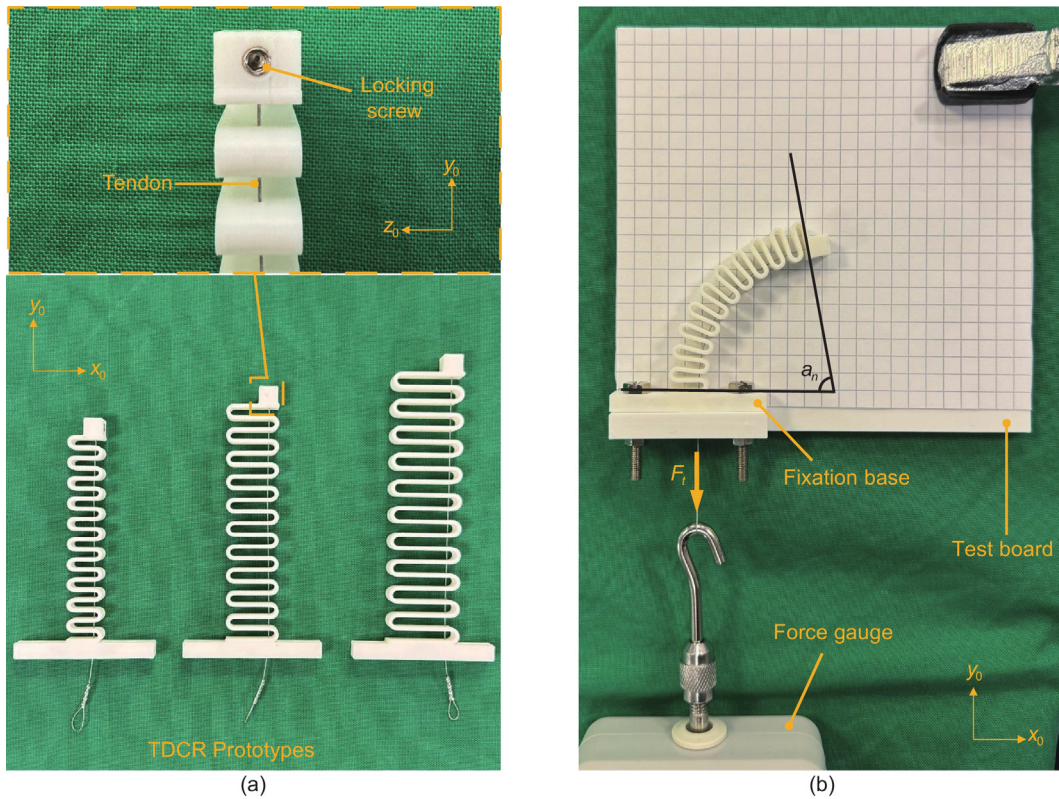


Fig. 5. (a) TDCR prototypes of various sizes. (b) Experimental setup for the bending test.

4. Experiments

4.1. Experimental setup

In this section, two separate experiments have been conducted, one to validate the model proposed before (Section 4.2) and another to assess the influence of structural parameters on the bending stiffness of TDCRs (Section 4.3). Since both experiments involved measuring the bending angles and tendon forces, they shared the same experimental setup, as shown in Fig. 5(b). The whole setup was composed of a force gauge (SF-500, Tripod Instrument Manufacturing Company, Ltd., China), a test board, and a TDCR prototype. As in Fig. 5(a), the TDCR prototype consisted of a single segment and included a fixation base at the bottom for attachment to the test board. A Polyamide 12 coated stainless-steel wire with an outer diameter of 0.36 mm (Carl Stahl GmbH, Germany) was used as material for tendons. The coating ensures minimal friction between the tendon and the backbone. Using a locking screw (see Fig. 5(a)), the tendon was fixed at its distal end to the TDCR backbone, while its proximal end had a loop knot secured by cord end terminals for easy connection to the hook of the force gauge. The bending motion of the TDCR was captured in photographs, while the tendon force F_t was simultaneously recorded by the force gauge. The generated bending angles θ_i were manually measured for each loading case. It is worth noting that the self-contact of the TDCR should be avoided while measuring, as the model does not take this factor into account.

4.2. Experimental validation of the kinematic model

This experiment aims to validate the kinematic model proposed in Section 3. During the experiment, the tendon force was smoothly increased to ensure a quasistatic state of the TDCR. We recorded the tendon forces and the corresponding bending angles

at three different time points as the measured data. Using the approach presented in Section 3.2, the data set with the lowest tendon force was used as input to the algorithm to calculate the bending stiffness of that TDCR. After that, the bending angles of that TDCR at the two remaining time points can be predicted by the model since we knew the value of the tendon forces from the measurement. By converting the bending angles to the bending shapes of all three TDCR prototypes, we obtained the results in Fig. 6.

The points in Fig. 6 represent the positions of the threading holes obtained according to Eq. (16) using measured and predicted bending angles. By connecting these points, we can visualize the bending shape of the TDCR prototype. It can be seen from Fig. 6 that the predicted and measured bending shapes are very similar. From this perspective, the performance of the proposed kinematic model is successfully validated. Nevertheless, it can still be noticed that there is a small amount of discrepancy between the simulated and measured bending shapes. One possible reason for this is that the TDCR prototype has undergone slight plastic deformation during the bending test. Although the proposed structure can largely avoid this issue, it is hard to entirely eliminate due to the inherently low yield strength of PLA, which eventually leads to the inaccuracy of the model.

4.3. Influence of structural parameters on bending stiffness

In this experiment, we investigated the influence of three structural parameters, the threading hole distance d , the line width t , and the inner radius r_{inner} on the bending stiffness of the TDCR. To ensure a fair comparison, fifteen TDCR prototypes were printed and subsequently divided into three groups based on the purposes. Each group contains five prototypes that differ solely in the structural parameter of interest. The spring constant K was used as an indicator of the bending stiffness since they are equivalent according to our model. A larger K indicates a higher

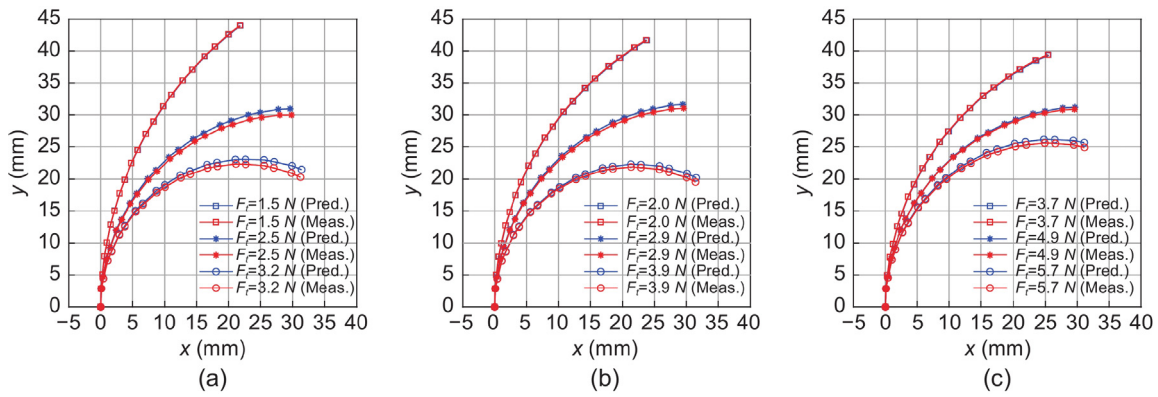


Fig. 6. Comparison between the predicted (Pred.) and measured (Meas.) bending shape of three different TDCR prototypes under varying tendon forces. (a) TDCR Prototype I. $R = 1.85$ mm, $a = 12.85$ mm, $b = 2.85$ mm. (b) TDCR Prototype II. $R = 1.95$ mm, $a = 12.95$ mm, $b = 2.95$ mm. (c) TDCR Prototype III. $R = 2.05$ mm, $a = 13.05$ mm, $b = 3.05$ mm.

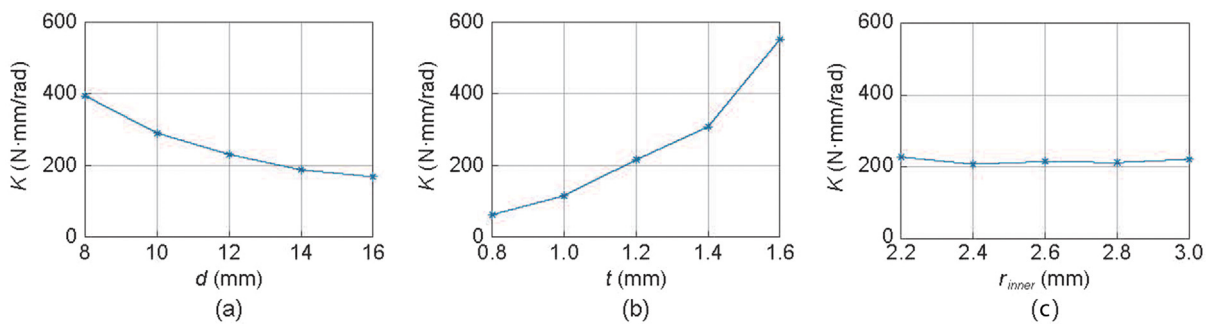


Fig. 7. Relations between bending stiffness and (a) the threading hole distance d , (b) the line width t , and (c) the inner radius r_{inner} .

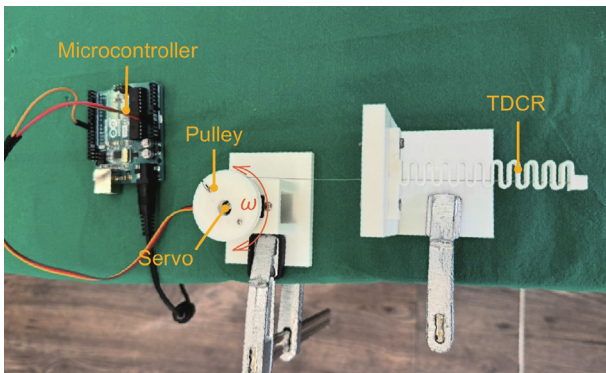


Fig. 8. Experimental setup for the hysteresis test.

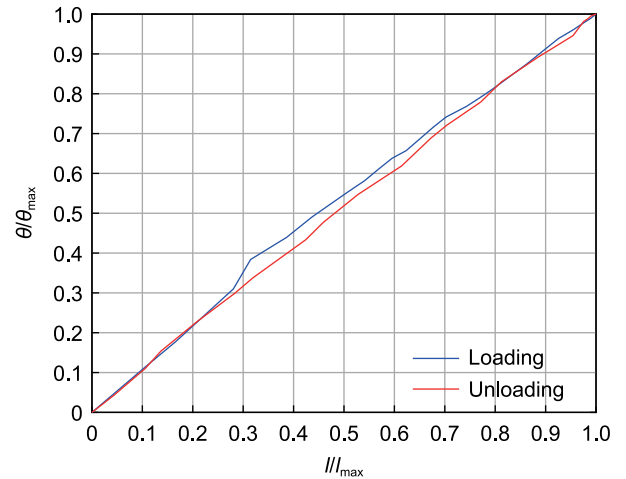


Fig. 9. Hysteresis curve of the proposed TDCR structure at a frequency of 0.5 Hz.

bending stiffness. To calculate the spring constants, experiments were carried out to measure the tendon forces and the resulting bending angles. The experimental results are presented in Fig. 7.

Fig. 7 illustrate the relation between K and the variables d , t , and r_{inner} . Fig. 7(a) shows that K decreases as the length d increases from 8 mm to 16 mm, with values dropping from approximately 400 N-mm/rad to about 150 N-mm/rad. Fig. 7(b) indicates a clear increasing trend of K with the line width t , rising significantly from around 50 N-mm/rad at 0.8 mm to approximately 550 N-mm/rad at 1.6 mm. Fig. 7(c) shows that K remains relatively stable, with minor fluctuations around 200–250 N-mm/rad as the inner radius r_{inner} varies from 2.2 mm to 3 mm. From this, we can conclude that TDCRs with small d and large t possess high bending stiffness, where t has a more significant influence on the bending stiffness than d . No obvious relation between r_{inner} and the bending stiffness can be observed.

4.4. Mechanical hysteresis

Cable hysteresis is a critical factor for tendon-driven continuum robotic structures [35]. Therefore, we have carried out cyclic load test to evaluate the mechanical hysteresis of the proposed TDCR structure. As presented in Fig. 8, the cyclic load was applied on the TDCR through a pulley, to which the proximal end of the tendon was fixed. The pulley was driven by a servo motor controlled by a microcontroller, allowing it to rotate back and forth within a specific angular range at a specified frequency. We chose 0.5 Hz for the tests because it is commonly encountered in our applications. The bending angles of the TDCR structure were

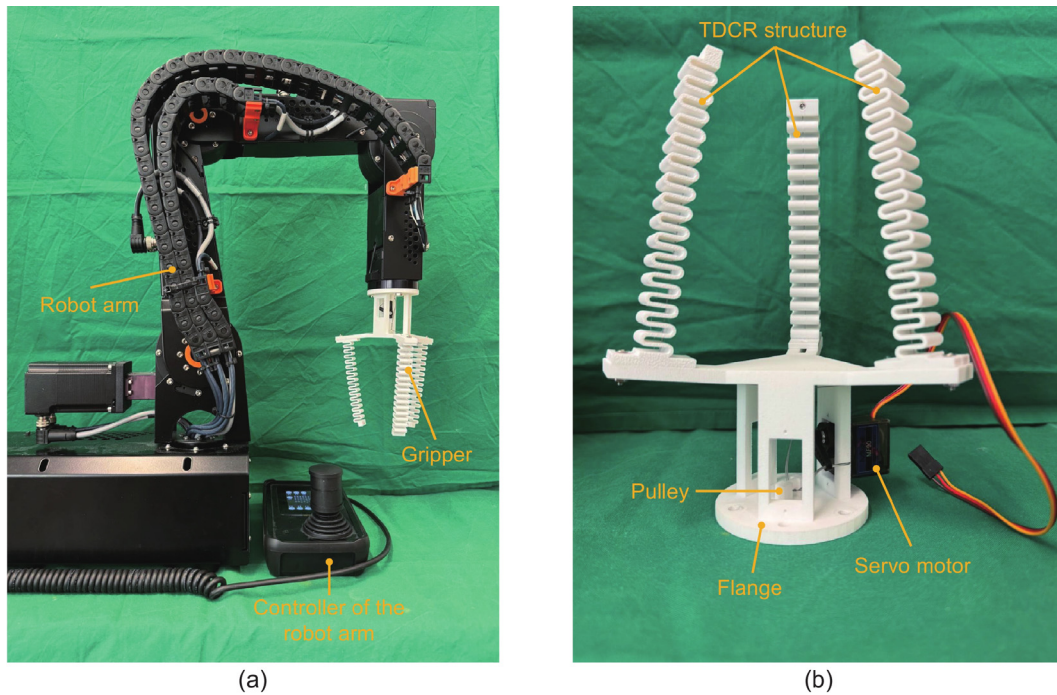


Fig. 10. (a) The setup of the demonstration. (b) The three-finger gripper.

measured for four load cycles, and the mean value of the angles during the loading and unloading processes was reported in Fig. 9.

Fig. 9 illustrates the relationship between relative tendon displacement and the relative bending angle of the structure. l_{\max} and θ_{\max} denote the maximum tendon displacement and the maximum bending angle during the load cycles, respectively. It can be observed that the hysteresis loop that occurred in the graph was quite small, indicating that the hysteresis effect of the proposed TDCR structure is negligible in normal operations. Nevertheless, possible reasons for the hysteresis phenomenon could be the system friction and the PLA material hysteresis.

4.5. Demonstration for possible application

In this section, we have built a three-finger gripper based on the proposed TDCR structure to demonstrate the possible application. As a proof-of-concept test, the bending motion of the continuum robotic structure was utilized to pick up several objects with different shapes (a spherical object, a 3D-printed middle ear model, a piece of 3D-printed cloth, and a dumbbell-shaped object) from the desk. As in Fig. 10(a), the three-finger gripper is mounted on a robot arm (igus robolink DCi, Commonplace Robotics GmbH, Germany) to realize a fully automated process. A servo motor (Miuzei MF90) is used to actuate the TDCR structures by pulling the tendons through a pulley (see Fig. 10(b)). Fig. 11 shows the states of the deformed TDCR structures at several time points. It can be seen that the tendons were loose when the gripper was open. As the tendons were pulled, the bending motions of the TDCR structures caused the fingers to contract and grasp the objects, which successfully demonstrated the possible gripper application of the continuum robotic structure. The detailed grasping processes can also be found in the supplementary video.

5. Discussion

The work presented in this article aims at developing a TDCR structure that can be fabricated using the FDM technique along

with its kinematic model. Using a serial S-shaped structure, a planar bending mechanism for the TDCR with minimum plastic deformation is realized. Compared to the rod-driven continuum robot using a staggered V-shaped notched structure in [36], where the shape of the bending segment is considered an ideal circular curve in its kinematic modeling, the kinematic model proposed in this paper does not rely on this assumption, which allows a more realistic prediction of the bending motion. On the other hand, unlike Feng et al. [37] used FEA to determine the mechanical properties of the 3D-printed TDCR, the NLP-based approach in our work greatly reduces computational cost and time. This allows the control algorithm to be executed by a micro-controller and thus enables embedded motion control. In addition, due to the advantages of the FDM technique the proposed TDCR can be fabricated in a very short time and requires no post-processing. For example, one finger of the aforementioned gripper took only around 15 min to print, which is much faster than the SLS-printed finger in [38].

Nevertheless, this work can still be improved in several aspects. For instance, the inverse kinematic of the proposed TDCR is difficult to obtain analytically. This problem can be solved by using machine learning, where the relation between tendon pulling length of the tendon and the corresponding bending angles of the TDCR. On the other hand, our model does not take external loads or friction into account. Self-contact between segments can also occur when the bending angle is large. Moreover, the degree of freedom of the TDCR was limited to one. Therefore, in future work, we plan to analyze the influence of external loads, friction and contacts, and further explore the potential of the proposed TDCR structure in various applications. Additionally, we will investigate the possibility of increasing the degrees of freedom based on this study.

6. Conclusion

In this article, we proposed an FDM-printable TDCR using a serial S-shaped structure. The PRBM-based kinematic model was presented to predict the bending motion under applied tendon

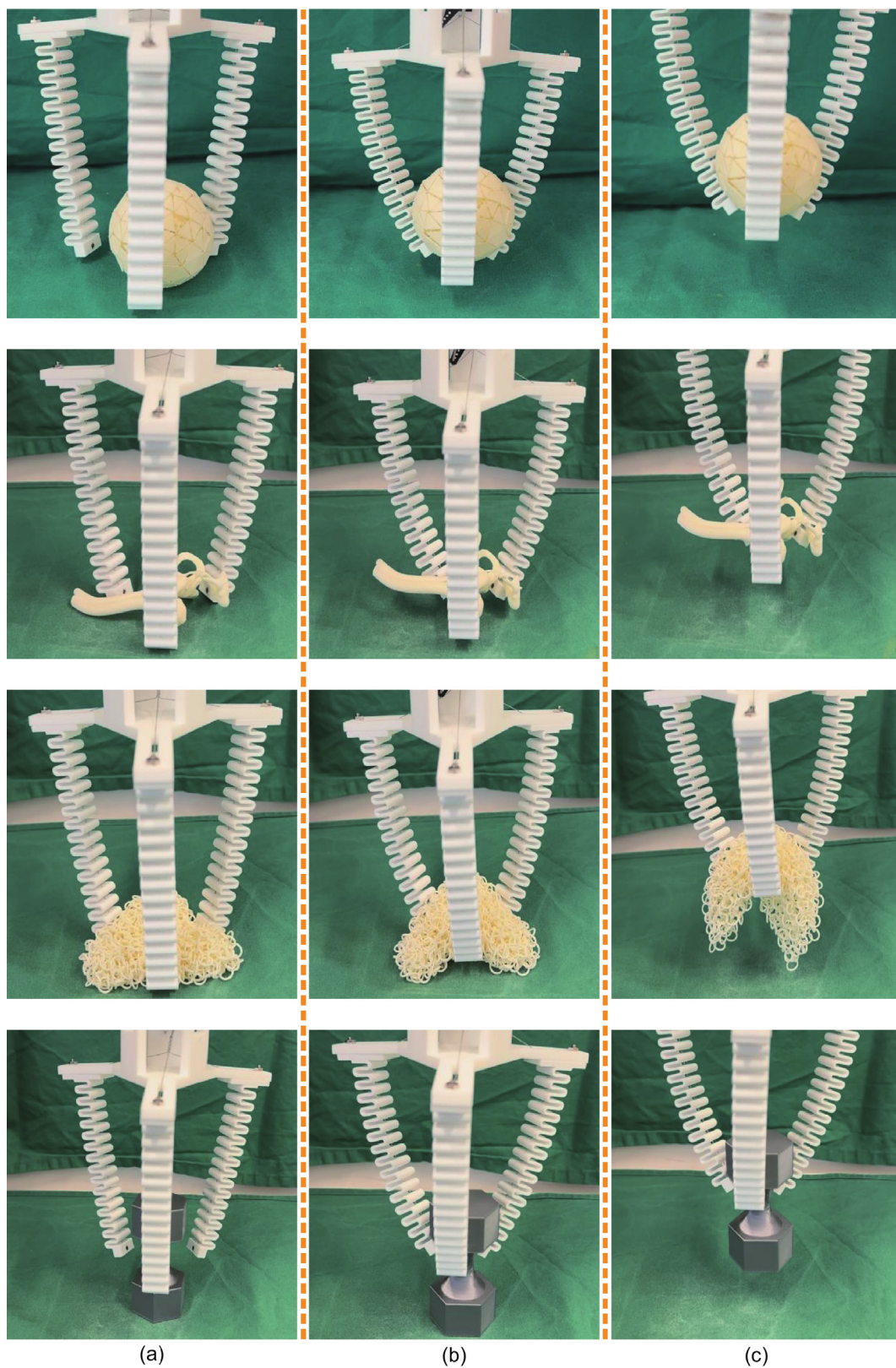


Fig. 11. Snapshots of the grasping process for different objects. (a) The tendons are loose and the gripper is open. (b) The tendons are pulled leading to the contraction of the gripper to grasp the object. (c) The robot arm moves upward while the tendons remain under tension.

force. The performance of the kinematic model was successfully validated through a series of bending tests. Several structural parameters were selected to assess their influence on the bending

stiffness. Experimental results showed that among them, varying the line width resulted in the largest change in the bending stiffness. Furthermore, it was experimentally demonstrated that

the effect of hysteresis is negligible in normal operations. Finally, a three-finger gripper was built to demonstrate the capability of the proposed TDCR structure in the real application.

CRedit authorship contribution statement

Kaidi Zhu: Writing – original draft, Validation, Software, Methodology, Investigation, Formal analysis. **Tim C. Lueth:** Funding acquisition. **Yilun Sun:** Writing – review & editing, Supervision, Project administration, Conceptualization, Funding acquisition.

Declaration of competing interest

The authors declare that they have no known competing financial interests or personal relationships that could have appeared to influence the work reported in this paper.

Acknowledgment

This research is supported by the teaching funding of TUM School of Engineering and Design.

Appendix A. Supplementary data

Supplementary material related to this article can be found online at <https://doi.org/10.1016/j.birob.2024.100188>.

References

- [1] T. da Veiga, J.H. Chandler, P. Lloyd, G. Pittiglio, N.J. Wilkinson, A.K. Hoshier, R.A. Harris, P. Valdastrì, Challenges of continuum robots in clinical context: a review, *Prog. Biomed. Eng.* 2 (3) (2020) 032003.
- [2] T. Li, G. Zhang, X. Li, X. Li, H. Liu, Y. Wang, Flexible head-following motion planning for scalable and bendable continuum robots, *Biomim. Int. Robotics* 4 (2) (2024) 100161.
- [3] T. Zheng, D.T. Branson, E. Guglielmino, D.G. Caldwell, A 3D dynamic model for continuum robots inspired by an octopus arm, in: 2011 IEEE International Conference on Robotics and Automation, IEEE, 2011, pp. 3652–3657.
- [4] J. Zhang, Y. Li, Z. Kan, Q. Yuan, H. Rajabi, Z. Wu, H. Peng, J. Wu, A pre-programmable continuum robot inspired by elephant trunk for dexterous manipulation, *Soft Robotics* 10 (3) (2023) 636–646.
- [5] Y. Peng, H. Nabae, Y. Funabara, K. Suzumori, Controlling a peristaltic robot inspired by inchworms, *Biomim. Intell. Robotics* 4 (1) (2024) 100146.
- [6] P.E. Dupont, N. Simaan, H. Choset, C. Rucker, Continuum robots for medical interventions, *Proc. IEEE* 110 (7) (2022) 847–870.
- [7] G. Zhang, F. Du, S. Xue, H. Cheng, X. Zhang, R. Song, Y. Li, Design and modeling of a bio-inspired compound continuum robot for minimally invasive surgery, *Machines* 10 (6) (2022) 468.
- [8] B. Ouyang, Y. Liu, D. Sun, Design of a three-segment continuum robot for minimally invasive surgery, *Rob. Biomim.* 3 (2016) 1–4.
- [9] J. Burgner-Kahrs, D.C. Rucker, H. Choset, Continuum robots for medical applications: A survey, *IEEE Trans. Robot. Autom.* 31 (6) (2015) 1261–1280.
- [10] Y. Yamauchi, Y. Ambe, H. Nagano, M. Konyo, Y. Bando, E. Ito, S. Arnold, K. Yamazaki, K. Itoyama, T. Okatani, et al., Development of a continuum robot enhanced with distributed sensors for search and rescue, *Robomech. J.* 9 (1) (2022) 8.
- [11] Y. Sun, F. Pancheri, C. Rehekampff, T.C. Lueth, TurBot: A turtle-inspired quadruped robot using topology optimized soft-rigid hybrid legs, *IEEE/ASME Trans. Mechatronics* 29 (4) (2024) 3193–3202.
- [12] M. Wang, X. Dong, W. Ba, A. Mohammad, D. Axinte, A. Norton, Design, modelling and validation of a novel extra slender continuum robot for in-situ inspection and repair in aeroengine, *Robot. Comput.-Integr. Manuf.* 67 (2021) 102054.
- [13] R.J. Webster, A.M. Okamura, N.J. Cowan, Toward active cannulas: Miniature snake-like surgical robots, in: 2006 IEEE/RSJ International Conference on Intelligent Robots and Systems, IEEE, 2006, pp. 2857–2863.
- [14] R.J. Webster, J.M. Romano, N.J. Cowan, Mechanics of precurved-tube continuum robots, *IEEE Trans. Robot.* 25 (1) (2008) 67–78.
- [15] Y. Kim, G.A. Parada, S. Liu, X. Zhao, Ferromagnetic soft continuum robots, *Sci. Robot.* 4 (33) (2019) eaax7329.
- [16] J. Edelmann, A.J. Petruska, B.J. Nelson, Magnetic control of continuum devices, *Int. J. Robot. Res.* 36 (1) (2017) 68–85.
- [17] K. Ikuta, H. Ichikawa, K. Suzuki, Safety-active catheter with multiple-segments driven by micro-hydraulic actuators, in: Medical Image Computing and Computer-Assisted Intervention—MICCAI 2002: 5th International Conference Tokyo, Japan, September 25–28, 2002 Proceedings, Part 1 5, Springer, 2002, pp. 182–191.
- [18] Z. Mao, Y. Peng, C. Hu, R. Ding, Y. Yamada, S. Maeda, Soft computing-based predictive modeling of flexible electrohydrodynamic pumps, *Biomim. Intell. Robotics* 3 (3) (2023) 100114.
- [19] S. Li, G. Hao, Current trends and prospects in compliant continuum robots: A survey, in: *Actuators*, vol. 10, MDPI, 2021, p. 145.
- [20] Y. Sun, Y. Liu, T.C. Lueth, Optimization of stress distribution in tendon-driven continuum robots using fish-tail-inspired method, *IEEE Robot. Autom. Lett.* 7 (2) (2022) 3380–3387.
- [21] Y. Chen, S. Yao, M.Q.-H. Meng, L. Liu, Chained spatial beam constraint model: A general kinetostatic model for tendon-driven continuum robots, *IEEE/ASME Trans. Mechatronics* (2024).
- [22] T. Wang, M.A. Post, A.M. Tyrrell, Twist: An agile compliant 3-dof tensegrity joint, *Biomim. Intell. Robotics* 4 (3) (2024) 100170.
- [23] Y. Sun, T.C. Lueth, Enhancing torsional stiffness of continuum robots using 3-D topology optimized flexure joints, *IEEE/ASME Trans. Mechatronics* 28 (4) (2023) 1844–1852.
- [24] Y. Sun, T.C. Lueth, Cruciate-ligament-inspired compliant joints: Application to 3D-printed continuum surgical robots, in: 2021 43rd Annual International Conference of the IEEE Engineering in Medicine & Biology Society, EMBC, IEEE, 2021, pp. 4645–4648.
- [25] Y. Sun, T.C. Lueth, Design of 3D-printed continuum robots using topology optimized compliant joints, in: 2023 IEEE International Conference on Soft Robotics (RoboSoft), 2023, pp. 1–6.
- [26] M.D. Kutzer, S.M. Segreti, C.Y. Brown, M. Armand, R.H. Taylor, S.C. Mears, Design of a new cable-driven manipulator with a large open lumen: Preliminary applications in the minimally-invasive removal of osteolysis, in: 2011 IEEE International Conference on Robotics and Automation, IEEE, 2011, pp. 2913–2920.
- [27] I. Gibson, D.W. Rosen, B. Stucker, M. Khorasani, D. Rosen, B. Stucker, M. Khorasani, Additive manufacturing technologies, vol. 17, Springer, 2021.
- [28] M. Attaran, The rise of 3-D printing: The advantages of additive manufacturing over traditional manufacturing, *Bus. Horiz.* 60 (5) (2017) 677–688.
- [29] J. Meyer-Szary, M.S. Luis, S. Mikulski, A. Patel, F. Schulz, D. Tretiakow, J. Fercho, K. Jaguszewska, M. Frankiewicz, E. Pawłowska, et al., The role of 3D printing in planning complex medical procedures and training of medical professionals—cross-sectional multispecialty review, *Int. J. Environ. Res. Public Health* 19 (6) (2022) 3331.
- [30] M. Chung, N. Radacsi, C. Robert, E.D. McCarthy, A. Callanan, N. Conlisk, P.R. Hoskins, V. Koutsos, On the optimization of low-cost FDM 3D printers for accurate replication of patient-specific abdominal aortic aneurysm geometry, *3D Print. Med.* 4 (2018) 1–10.
- [31] H.K. Dave, J.P. Davim, Fused Deposition Modeling Based 3D Printing, Springer International Publishing, 2021.
- [32] L.L. Howell, S.P. Magleby, B.M. Olsen, J. Wiley, Handbook of Compliant Mechanisms, Wiley Online Library, 2013.
- [33] Y. Sun, T.C. Lueth, Safe manipulation in robotic surgery using compliant constant-force mechanism, *IEEE Trans. Med. Robotics Bionics* 5 (3) (2023) 486–495.
- [34] Y. Sun, D. Zhang, Y. Liu, T.C. Lueth, Fem-based mechanics modeling of bio-inspired compliant mechanisms for medical applications, *IEEE Trans. Med. Robotics Bionics* 2 (3) (2020) 364–373.
- [35] H.-J. Yu, W.-L. Yang, Z.-X. Yang, W. Dong, Z.-J. Du, Z.-Y. Yan, Hysteresis analysis of a notched continuum manipulator driven by tendon, *Mech. Sci.* 9 (1) (2018) 211–219.
- [36] Y. Xu, D. Song, Z. Zhang, S. Wang, C. Shi, A novel extensible continuum robot with growing motion capability inspired by plant growth for path-following in transoral laryngeal surgery, *Soft Robotics* 11 (1) (2024) 171–182.
- [37] F. Feng, W. Hong, L. Xie, Design of 3D-printed flexible joints with presettable stiffness for surgical robots, *IEEE Access* 8 (2020) 79573–79585.
- [38] Y. Sun, Y. Liu, F. Pancheri, T.C. Lueth, LARG: A lightweight robotic gripper with 3-D topology optimized adaptive fingers, *IEEE/ASME Trans. Mechatronics* 27 (4) (2022) 2026–2034.